Numerical Assessment of Thermal Performance in Hollow Clay Masonry: Continuous Insulation Layers versus Partial Cavity Fills

Ahlam Alaoui [1]*, Muamer Kadic [2], Sébastien Guenneau [3], Mohammed Lahsaini [1] , and Younes Achaoui [1]

[1]Laboratory of Optics, Information Processing, Mechanics, Energetics and Electronics, Department of Physics, Moulay Ismail University, B.P. 11201, Zitoune, Meknes, Morocco
[2]Université de Franche-Comté, Institut FEMTO-ST, UMR6174, CNRS, 25000 Besançon, France
[3]The Blackett Laboratory, Physics Department, Imperial College, London, SW7 2AZ, UK

Abstract. This study presents a comparative analysis of thermal retrofit strategies for hollow-clay-brick walls under high-intensity summer conditions. A numerical model coupling conduction, convection, and radiation simulates six configurations: an uninsulated wall, systems with 50 mm continuous extruded polystyrene (XPS) layers (external/internal), and full and partial cavity fills. The model is driven by a diurnal cycle with high ambient temperatures (25–45 °C) and significant solar irradiance. Results demonstrate a pronounced performance gradient. The continuous XPS layers are most effective, reducing thermal transmittance by 74% and providing superior dynamic performance. External XPS yields the largest thermal lag and smallest indoor swing while internal XPS offers comparable amplitude reduction. All cavity-fill strategies provide more modest U-value reductions (12–13%) and dynamic behavior similar to the reference wall. This work provides a critical dataset for selecting insulation strategies, concluding that continuous layers are optimal for peak performance, while cavity fills offer a viable supplementary or alternative solution where architectural constraints apply.

1 Introduction

In summer-dominant climates, the envelope's most consequential attributes are time-dependent: how it attenuates the daily heat wave and how far it shifts that wave in time. These behaviours are described by two complementary metrics—the decrement factor (amplitude attenuation) and the phase shift or time lag (temporal delay)—which complement the steady-state U-value. Within this framework, Lu et al. derive analytical expressions for walls subjected to sinusoidal outdoor excitation, yielding explicit formulas for both metrics and a

* Corresponding author: ahla.alaoui@edu.umi.ac.ma

rigorous basis for interpreting diurnal simulations and design decisions [1]. In a complementary vein, Özel demonstrates that insulation location in multilayer walls decisively alters time lag and decrement factor, and further offers an optimization framework for thickness under periodic loading—directionally favouring exterior placement when summer dynamics dominate [2].

Focusing on the hollow-brick typology itself, Vera et al. examine structural hollow clay bricks and report tangible reductions in U-value by tuning clay/mortar conductivities and grid geometry; however, their results underscore that the continuous ceramic webs and mortar bridges remain influential heat-flow paths unless a truly continuous thermal barrier is introduced [3].

Beyond conventional layers, Gao and Meng survey phase-change-material (PCM) integration in bricks and conclude that properly selected PCM (melting range and mass fraction) can dampen daily temperature swings and shift loads, while stressing sensitivities to placement within the unit and long-term stability [4]. At the façade scale, Zhang et al. review switchable (adaptive) building envelopes—from thermo-optical skins to airflow-regulated assemblies—and quantify the energy-saving potential of modulating envelope properties to better align with diurnal demand patterns [5].

Turning to the role of mass, Salehpour et al. show, through coupled simulations at room and building levels, that thermal mass magnitude and placement materially influence transient wall response and operational energy. Their findings reinforce the best practice of placing structural mass inside the insulation in summer climates. [6]. In terms of operation, Xu et al. analyse exterior walls under intermittent air-conditioning, demonstrating how start-up transients and layer ordering shape early-time wall performance in a hot-summer/cold-winter climate—insights that translate to broader diurnal analyses [7].

Within the hollow-brick context, Hou et al. experimentally and numerically assess cavity filling with insulation under intermittent HVAC, finding measurable but bounded improvements when solid bridges persist—i.e., suppressing intra-cavity convection alone cannot fully offset conduction through webs and joints [8]. To clarify the physics inside cellular enclosures, Mikhailenko et al. resolve coupled thermal radiation and natural convection in a large-scale honeycomb analogue, identifying regimes where radiation is non-negligible versus those where conduction–convection dominates [9].

Design innovation at the unit scale also matters. Chen and Liu present numerical prototyping and optimization of raw-earth energy-saving hollow bricks, linking perforation patterns and material selection to thermal performance and offering a systematic path from concept to product [10]. From an experimental-numerical perspective on composite envelopes, Nath et al. provide and validate a U-value determination approach for a novel wall assembly, illustrating robust procedures for benchmarking simulated and measured performance [11]. Regionally, Bachir and Taieb optimize hollow-brick roofing for a hot climate, showing that configuration choices (geometry, materials) measurably affect energy performance and thermal stress at roof level—an insight extensible to vertical façades [12]. At the building scale, Zheng et al. optimize exterior insulation thickness by orientation, quantifying economic, energy and carbon outcomes and thereby embedding envelope decisions within a wider sustainability calculus [13]. Finally, Yang and Chen analyse a pipe-embedded, thermally diffusive wall system, demonstrating notable dynamic damping and energy-saving potential—a reminder that dynamic metrics (phase shift, flux attenuation) are decisive beyond steady U-values [14].

Despite this rich literature, studies typically consider either (i) continuous insulation layers (exterior vs interior) or (ii) cavity-filling schemes (full or partial)—rarely both within the same experimental–numerical framework using identical geometry, properties, film coefficients, and analytic diurnal forcings while reporting both interior-surface temperature and interior heat-flux waveforms over a full 24-hour cycle. This separation is especially striking given the current enthusiasm for filling brick cavities with foams or alternative materials for energy efficiency. The present work directly answers that need: we place continuous layers (outside versus inside) and cavity fills (full and half) side-by-side on the same eight-hole hollow-brick panel, under shared steady and diurnal boundary conditions, to reveal how these strategies differ in amplitude reduction and phase behaviour at the room side.

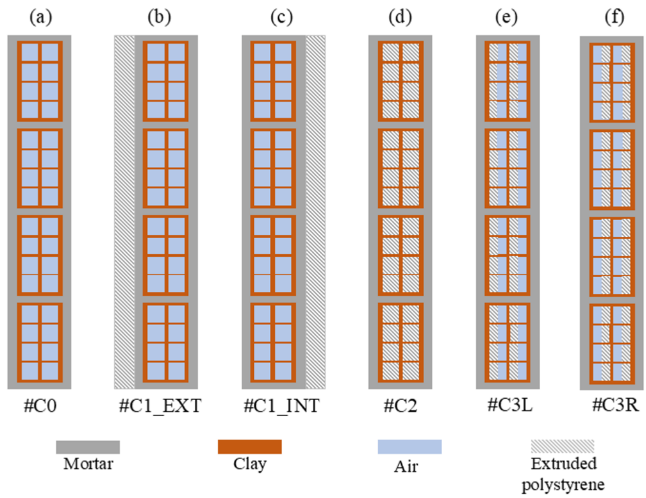

Fig. 1. Cross-sectional views of the simulated hollow clay brick wall configurations: (a) Uninsulated reference (C0); (b) External 50 mm XPS insulation (C1_EXT); (c) Internal 50 mm XPS insulation (C1_INT); (d) Full cavity fill (C2); (e) Half-cavity fill, left orientation (C3L); (f) Half-cavity fill, right orientation (C3R). Materials are denoted by their respective patterns.

2 Materials and method

2.1 Wall typologies and configurations

Finite-element analysis is carried out on a two-dimensional macro-element consisting of four hollow clay bricks separated by 10 mm mortar joints (bed and head). Each brick has a thickness (wall depth) of 100 mm and a height of 260 mm; its internal geometry comprises eight rectangular cavities arranged in a 2×4 array, each cavity measuring 35 mm × 50 mm. Six wall configurations are investigated (Fig. 1): C0, the reference brickwork with unfilled cavities; C1_EXT, the same wall fitted with a 50 mm continuous extruded-polystyrene (XPS) layer on the exterior face; C1_INT, with a 50 mm continuous XPS layer on the interior face; C2, in which all cavities are fully filled with XPS; C3L, where each cavity is half-filled on its left half-section with XPS; and C3R, where each cavity is half-filled on its right half-section with XPS.

2.2 Governing physics and numerical formulation

2.2.1 Assumptions

All solid phases (red clay, mortar, and extruded polystyrene) are modeled as homogeneous, isotropic, and temperature-independent media over the investigated range; their thermophysical triplet (k, C_p, ρ) is reported in Table 1. The air contained in the cavities is treated as a Newtonian, incompressible fluid in laminar regime, with buoyancy introduced via the Boussinesq approximation, i.e. density departures from a reference value ρ_0 are accounted for only in the gravitational body-force term. Surfaces are diffuse–gray for thermal radiation.

Table 1. Thermophysical properties of the materials used in the numerical simulations.

Material	Thermal conductivity (W/m.K)	Heat capacity (J/kg.K)	Density (kg/m³)
Red clay	0.54	775	1810
Mortar	0.613	1701	1650
Extruded polystyrene	0.027	1210	55

2.2.2 Mathematical model

i. Conservation of mass, momentum and energy

In the fluid (air cavities):

$$\nabla \cdot u = 0 \tag{1}$$

$$\rho_0 \left(\frac{\partial u}{\partial t} + u . \nabla u \right) = -\nabla p + \mu \nabla^2 + \rho_0 \beta (T - T_0) g \tag{2}$$

$$\rho_f C_{p,f} \left(\frac{\partial T}{\partial t} + u . \nabla T \right) = \nabla . (k_f \nabla T) \tag{3}$$

In the solids (bricks, mortar, XPS):

$$\rho_s C_{p,s} \frac{\partial T}{\partial t} = \nabla . (k_s \nabla T) \tag{4}$$

Here u is velocity, p pressure, T temperature, μ viscosity, β the thermal expansion coefficient (Boussinesq) and T_0 a reference temperature.

Boussinesq approximation:

Density variations are neglected everywhere except in the buoyancy term: $\rho=\rho_0[1-\beta(T-T_0)]$, which leads to the body-force term in (Eq.2).

ii. Thermal radiation (radiosity formulation)

For an enclosure of N diffuse–gray surfaces, the radiosity J_i (Wm^{-2}) of surface i satisfies

$$J_i = \varepsilon_i \sigma T_i^4 + (1-\varepsilon_i)\sum_{j=1}^{N} F_{ij} J_j \tag{5}$$

where ε_i is emissivity, σ the Stefan–Boltzmann constant, and F_{ij} the view factor $\sum_j F_{ij}=1$. The net radiative heat flux leaving i is

$$q''_{\mathrm{rad},i} = J_i - \sum_{j=1}^{N} F_{ij} J_j \tag{6}$$

iii. Initial and boundary conditions (heat exchange)

- Initial condition :

$$T(x,0) = 20°C$$

- Interior surface: Natural convection to indoor air:

Let $T_{s,\mathrm{ext}}$ and $T_{s,\mathrm{int}}$ be the outer/inner surface temperatures; n is the outward normal.

$$-k\nabla T.n = h_i(T_{s,int} - T_i), \quad h_i = 8\ W\ m^{-2}k^{-1},\ \ T_i = 26°C \tag{7}$$

- Exterior surface : Convection to outdoor air plus short-wave solar loading:

$$-k\nabla T.n = h_e\left(T_{s,ext} - T_{ext}(t)\right) + \alpha\ I(t), \quad h_e = 20\ W\ m^{-2}k^{-1}, \alpha = 0.6 \tag{8}$$

Steady-state runs: T_{ext}= 45 °C and I(t)=0.

Transient runs (24 h): $T_{ext}(t)$ and I(t) are given analytically below.

iv. Diurnal forcings (analytic forms)

Let t be time in seconds and define the diurnal hour

$$\tau = \frac{mod(t, 86400)}{3600} \in [0,24] \tag{9}$$

Outdoor temperature and short-wave irradiance used in this study are prescribed analytically as

$$T_{ext}(\tau) = \bar{T} + A\,sin(\tfrac{2\pi}{24}(\tau - 12)), \bar{T} = 35°C, A = 10°C \quad (10)$$

$$I(\tau) = I_{max} exp\,[-a(\tau - 12)^2], I_{max} = 1000\,Wm^{-2},\ a = 0.06\,h^{-2} \quad (11)$$

v. Performance metrics

At steady state, the area-averaged heat flux through the wall is $\bar{q}''$(positive from exterior to interior). The overall thermal resistance and the transmittance are

$$R = \frac{\Delta T}{\bar{q}''} \text{ and } U = \frac{1}{R} \quad (12)$$

With $\Delta T = T_i - T_{ext,ref}$ (indoor air minus outdoor reference), units R [m^2KW^{-1}] and U [$Wm^{-2}K^{-1}$].

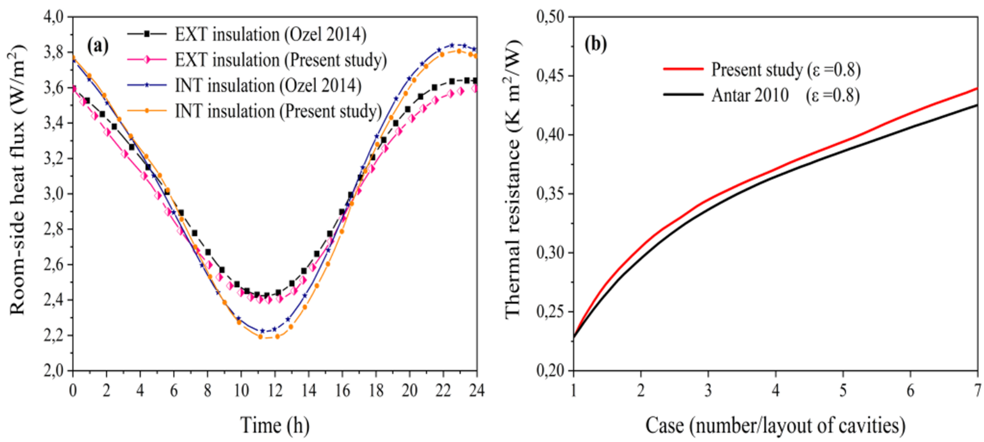

Fig. 2. Validation against the literature. (a) Room-side heat flux on 15 July for identical walls with exterior (EXT) and interior (INT) insulation: present study against Ozel [2]. (b) Overall thermal resistance (R-value) for cavity cases (1–7) at thermal emissivity of ε=0.8: present study against Antar [15].

2.3 Validation of the numerical model

The model was confronted with two benchmark tests that bracket our physics. First, following Ozel [2], we reproduced a laminated wall under diurnal forcing (15 July) for exterior (EXT) and interior (INT) insulation, using the same layer stack, thermophysical properties, film coefficients, and sol-air formulation. The room-side heat-flux waveform over 24 h matches the reference closely: the morning trough near 10–12 h, the afternoon rebound, and the evening crest around 22–24 h are all captured, while the expected ordering is preserved; EXT yields a smaller daily swing and a larger phase delay than INT. Amplitude differences remain within a few percent; peak times agree to < 1 h. Second, following Antar [15], we simulated a 2-D hollow clay block with isothermal vertical sides, adiabatic horizontal edges, Boussinesq air in the cavities, and diffuse–gray radiosity at ε=0.8. The overall thermal resistance $R=\Delta T/q_{net}$ increases monotonically with the number/layout of cavities (cases 1–7), and our curve tracks the reference with a small, consistent positive bias of about 2–5 % plausibly due to minor differences in film evaluation, corner idealization (view factors), or the radiosity coupling. Taken together, these checks indicate that the solver reliably predicts both the layer-ordering dynamics of laminated walls and the combined conduction–convection–radiation mechanisms that govern hollow-brick heat transfer.

3 Results and discussion

3.1 Steady-state response (Thermal resistance and transmittance)

Under steady boundary conditions (exterior 45 °C; interior 26 °C; h_e=20 $Wm^{-2}K^{-1}$, h_i=8 $Wm^{-2}K^{-1}$), the six wall variants exhibit a clear, reproducible hierarchy in overall thermal resistance R and transmittance U=1/R (numerical values in Table 2). The reference masonry (C0) yields R=0.6635 m^2KW^{-1} and U=1.507 $Wm^{-2}K^{-1}$, which we take as the baseline for comparison. Adding a continuous 50 mm XPS layer produces the largest step-change: C1_EXT and C1_INT reach R=2.5624 and 2.5608 m^2KW^{-1}, respectively, corresponding to U≈0.390 $Wm^{-2}K^{-1}$ and a ∼74% reduction in heat transmission relative to C0. The near-identity of U for exterior versus interior placement is expected at steady state, because—in the absence of thermal storage effects—the total resistance is governed by the sum of film and layer resistances; re-ordering layers of identical thickness and conductivity leaves R essentially unchanged. A useful way to appreciate the scale of the improvement is to normalize by the baseline: R/R_{C0} ≈3.86 for both C1 variants, i.e. almost a four-fold increase in resistance.

Table 2. Thermal resistance (R-value) and transmittance (U-value) for each configuration, including the percentage reduction in U-value relative to the uninsulated case (C0).

Configuration	R ($m^2\cdot K\cdot W^{-1}$)	U=1/R ($W\cdot m^{-2}\cdot K^{-1}$)	ΔU vs C0
C0	0.6635	1.507	–
C1_EXT (50 mm XPS outside)	2.5624	0.390	−74.1 %
C1_INT (50 mm XPS inside)	2.5608	0.391	−74.1 %
C2 (full cavity fill)	0.7544	1.326	−12.0 %
C3L (half-fill, left)	0.7638	1.309	−13.1 %
C3R (half-fill, right)	0.7640	1.308	−13.2 %

By contrast, strategies that fill the cavities with insulation—without creating a continuous external barrier—deliver only modest gains. The full-fill case C2 gives R=0.7544 m^2KW^{-1} (U=1.326 $Wm^{-2}K^{-1}$), i.e. a ∼12% reduction in U versus C0. Physically, once natural convection in the voids is suppressed by the solid infill, the residual heat flow is dominated by continuous ceramic webs and mortar bridges, which remain efficient conductive paths; the added XPS acts locally but does not interrupt these solid networks that span the wall thickness. The half-fill variants C3L and C3R perform marginally better than C2 (R≈0.764 m^2KW^{-1}, U≈1.309 $Wm^{-2}K^{-1}$; ~13% reduction vs C0). This small edge is consistent with a picture in which partitioning each cavity with a partial infill disrupts the dominant conduction pathways across the void cross-section and retains a thin quiescent air sub-layer whose effective conductivity is comparable to that of XPS; the net series/parallel mix across the section can therefore be slightly more resistive than a fully filled cell. The left–right asymmetry (C3L vs C3R) is indistinguishable in steady state (ΔR<0.03 %), as expected when only the integrated conductive network matters.

An additional point reinforce the robustness of these rankings. Film resistances account for R_{films}= $1/h_e+1/h_i$ = 0.050+0.125 =0.175 m^2KW^{-1}. In the high-performance cases (C1), films represent only ~7 % of R_{total} (0.175/2.56), so moderate variations in h_e or h_i have little influence on U. In the baseline (C0), films are a much larger ~26 % share (0.175/0.6635), explaining why uninsulated walls are more sensitive to external wind/indoor convection assumptions.

Overall, the steady-state evidence is unambiguous: only the continuous 50 mm XPS layer drives U into the sub-0.4 W m^{-2} K^{-1} regime associated with high-performance façades, whereas cavity-based interventions—full or partial—recover at most a low-teens percentage of improvement because they do not sever the solid conduction skeleton of the masonry. This conclusion sets the stage for the transient analysis, where insulation placement (exterior vs interior) no longer remains equivalent and the dynamic response (temperature swing and phase shift at the room-side surface) becomes the decisive metric.

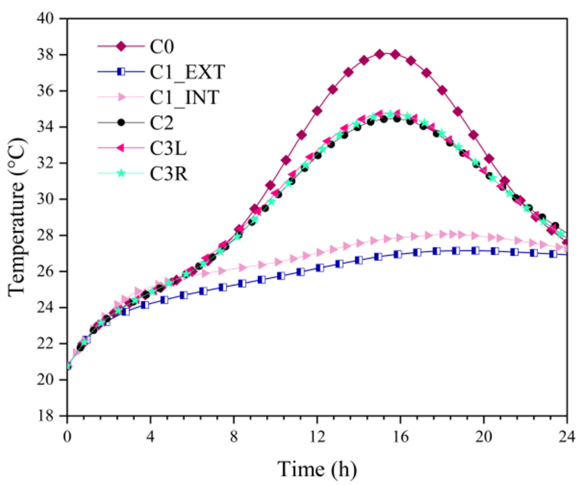

Fig. 3. Inner surface temperature evolution. External XPS (C1_EXT) provides the largest phase lag and smallest amplitude. Internal XPS (C1_INT) offers similar attenuation with an earlier peak. Cavity fills (C2, C3L, C3R) show negligible improvement over the uninsulated wall (C0).

3.1 Transient response under diurnal forcing

When the exterior face is driven by the analytic summer-day signals—a sinusoidal outdoor air temperature (25–45 °C) superposed with a noon-peaked short-wave irradiance (1000 W m^{-2})—the six wall variants display markedly different time–domain behaviours at the room side (Fig. 3: Ts,int(t); Fig. 4: Qin(t)). Two robust features emerge. First, the continuous insulation solutions (C1_EXT, C1_INT) compress both the daily temperature swing and the heat-flux amplitude at the indoor surface to a narrow band compared with the uninsulated reference (C0). Second, exterior placement of the same 50 mm XPS (C1_EXT) yields a later and lower interior response than interior placement (C1_INT), despite their indistinguishable steady-state U values.

3.1.1 Temperature response

Relative to C0, all insulated cases depress the daytime peak of $T_{s,int}(t)$ and elevate the nighttime trough, but the ranking is clear: C1_EXT exhibits the smallest daily swing and the largest phase delay (latest occurrence of the maximum), followed by C1_INT; the cavity-based options (C2 full fill; C3L/C3R half fills) sit in a middle band, with curves that remain visibly closer to C0. The mechanism is classical. With external insulation, the high-capacity clay–mortar core is kept inside the insulated envelope; under a 24 h excitation, the thermal penetration depth in clay ($\delta \simeq 2\alpha P/\pi$) is of order 14–15 cm for the adopted properties, i.e. comparable to or exceeding the brick thickness. The wall therefore acts as a low-pass, phase-shifting filter: the XPS layer damps the high-frequency content carried by solar spikes, while the retained masonry mass stores and releases heat over the cycle, pushing the interior peak into the evening. With interior insulation, by contrast, the inner surface is essentially the XPS skin—which has negligible heat capacity—so the room-side temperature is protected in amplitude but reacts sooner to the external drive: the phase shift is reduced because the masonry mass is now largely outside the insulated envelope and cannot contribute to buffering on the room side. The cavity fills (C2/C3L/C3R) suppress buoyant recirculation in the voids but do not sever the continuous ceramic webs and mortar bridges; as a result, their dynamic attenuation of $T_{s,int}(t)$ remains limited, and their peaks occur earlier than with C1_EXT.

3.1.2 Heat-flux response

The interior heat-flux signals $Q_{in}(t)$, depicted in Fig.4, mirror the temperature trends but reveal an additional nuance: C1_EXT not only minimizes the peak magnitude but also spreads the inward heat release over a broader portion of the evening/night, indicative of genuine thermal storage in the masonry core followed by delayed discharge to the room. C1_INT delivers a similar average reduction in daily heat intake, yet with a narrower peak and earlier zero-crossings, consistent with a lower effective thermal admittance at the room side when the inner lining is low-capacity XPS. In the cavity-based cases, the amplitude of $Q_{in}(t)$ is cut only modestly compared with C0; the waveforms retain a sun-synchronous character with a mid-afternoon dominance, underscoring again that removing air-side convection in the holes is insufficient as long as the solid conduction skeleton of the brickwork remains intact. Within plotting resolution, C3L and C3R are indistinguishable, confirming that left/right half-fill orientation has no practical effect on the room-side dynamics for the adopted vertical-cavity geometry.

https://doi.org/10.1051/e3sconf/202568000070

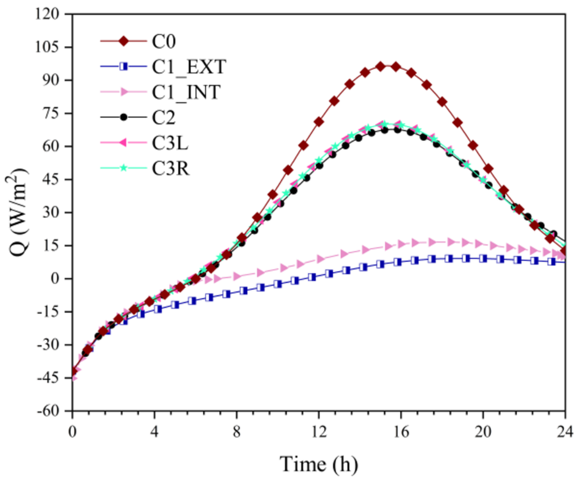

Fig. 4. Inner surface heat flux. Negative values indicate heat gain. External XPS (C1_EXT) minimizes cooling load significantly. The performance of cavity fills is nearly identical to the uninsulated case.

4 Conclusion

This comprehensive study demonstrates that the thermal performance of hollow clay brick walls under high-intensity summer conditions is profoundly influenced by insulation strategy, with steady-state and transient analyses converging on a clear hierarchy of efficacy. The application of a continuous 50 mm extruded polystyrene (XPS) layer delivers a transformative improvement, slashing the thermal transmittance by 74% from 1.507 W m^{-2} K^{-1} to approximately 0.39 W m^{-2} K^{-1}; externally applied XPS proves dynamically superior, maximizing thermal lag and minimizing indoor temperature swings to effectively mitigate cooling loads, while interior XPS, though achieving an identical U-value reduction, induces a faster thermal response due to its isolation of the wall's thermal mass. In stark contrast, cavity-fill strategies—whether fully or partially filling the voids—offer only a marginal benefit, reducing the U-value by a modest 12-13% to around 1.32 W m^{-2} K^{-1}, as their primary mechanism of suppressing convective heat transfer is ultimately constrained by the persistent conductive pathways through the solid brick webs and mortar joints, resulting in dynamic behavior nearly indistinguishable from the uninsulated reference wall and rendering the orientation of partial fills an insignificant factor. Consequently, while continuous exterior XPS is unequivocally the optimal strategy for maximizing energy efficiency and thermal comfort, interior XPS serves as a competent alternative for retrofit scenarios with façade constraints, and cavity fills must be viewed strictly as a supplementary measure for contexts where minimal intervention is the paramount concern.

Acknowledgements

We would like to thank the Moroccan Ministry of Higher Education, Scientific Research and Innovation, the OCP Foundation, the UM6P, and the CNRST for supporting this work through the APRD research program. We also gratefully acknowledge the scholarship from the CNRST through the Excellence Scholarship Program to A.Alaoui.

References

1. Y. Lu, J. Hu, J. Yu, L. Yuan, K. Bao, Appl. Therm. Eng. **242**, 122487 (2024)
2. M. Özel, Energy Build. **72**, 288–295 (2014)
3. S. Vera, C. Figueroa, S. Chubretovic, J.C. Remesar, F. Vargas, Constr. Build. Mater. **415**, 135060 (2024)
4. Y. Gao, X. Meng, J. Energy Storage **62**, 106913 (2023)
5. G. Zhang, H. Wu, J. Liu, Y. Liu, Y. Ding, H. Huang, Renew. Sustain. Energy Rev. **202**, 114716 (2024)
6. B. Salehpour, M. Ghobadi, H. Ge, T. Moore, J. Build. Phys. **47**(1), 92–120 (2023)
7. L. Xu, Y. Ding, C. Du, J. Build. Eng. **95**, 110204 (2024)
8. C. Hou, X. Meng, Y. Gao, W. Mao, E. Long, Case Stud. Constr. Mater. **8**, 217–225 (2018)
9. S.A. Mikhailenko, I.V. Miroshnichenko, M.A. Sheremet, Build. Simul. **14**(3), 681–691 (2021)
10. R. Chen, H. Liu, J. Build. Eng. **70**, 106456 (2023)
11. B. Nath, S. Roy, B. Das, M.A. Ehyaei, Therm. Sci. Eng. Prog. **53**, 102751 (2024)
12. A. Bachir, N. Taieb, Constr. Build. Mater. **367**, 130336 (2023)
13. Z. Zheng, J. Xiao, Y. Yang, F. Xu, J. Zhou, H. Liu, Energy **290**, 130300 (2024)
14. Y. Yang, S. Chen, Build. Simul. **16**(12), 2285–2305 (2023)
15. M.A. Antar, Energy **35**, 3508–3516 (2010)